

Linear Revolution-Invariance: Modeling and Deblurring Spatially-Varying Imaging Systems

Amit Kohli*, Anastasios Angelopoulos*, Sixian You, Kyrollos Yanny, Laura Waller

June 20, 2022

Abstract

We develop theory and algorithms for modeling and deblurring imaging systems that are composed of rotationally-symmetric optics. Such systems have point spread functions (PSFs) which are spatially-varying, but only vary radially, a property we call *linear revolution-invariance* (LRI). From the LRI property we develop an exact theory for linear imaging with radially-varying optics, including an analog of the Fourier Convolution Theorem. This theory, in tandem with a calibration procedure using Seidel aberration coefficients, yields an efficient forward model and deblurring algorithm which requires only a single calibration image—one that is easier to measure than a single PSF. We test these methods in simulation and experimentally on images of resolution targets, rabbit liver tissue, and live tardigrades obtained using the UCLA Miniscope v3. We find that the LRI forward model generates accurate radially-varying blur, and LRI deblurring improves resolution, especially near the edges of the field-of-view.

1 Introduction

The ability to mathematically model an imaging system is a fundamental tool for designing, analyzing, and correcting it. This is typically done by measuring point spread functions (PSFs): images of point sources which characterize an imaging system’s behavior across its field-of-view (FoV). A *forward model* then specifies how these PSFs are used to calculate the output image. It is common to assume the PSFs are the same everywhere in the FoV, in which case the system is linear shift-invariant (LSI) and we can model the output as a convolution of the scene and the center PSF. This assumption is often inaccurate and can lead to poor approximations of systems whose PSFs are shift-varying across the FoV; however, without any assumptions, the forward model becomes infeasible to compute. In this paper, we recognize that most optics are rotationally-symmetric and leverage the symmetry this imposes on their PSFs to obtain a simple, fast, and exact forward model, which we use for image deblurring.

Our method relies on a property we call *linear revolution-invariance* (LRI), which states that when a point source revolves around the optical axis at a fixed radius, the corresponding PSF also revolves without changing shape. Under LRI, knowledge of one PSF at a particular radius is sufficient to know all the PSFs at that radius. Note that each PSF itself is *not* necessarily rotationally-symmetric. Any system composed of rotationally-symmetric optics centered on the optical axis is LRI. Thus, the LRI property encompasses a large class of practical imaging systems. By utilizing the special behavior of an LRI system’s PSFs, we develop practical, theoretically exact algorithms for forward modeling and deblurring shift-varying LRI imaging systems without resorting to infeasible or approximate forward models (e.g., local convolutions).

One can compose a linear forward model of an imaging system by superimposing its PSFs from each object point in the FoV. In the LSI case, each PSF is identical and so any single PSF suffices to compute the forward model. However, for accurate modeling of shift-varying systems one would need to measure the PSF from every point in the FoV. This practically incurs significant complication, requiring motion stages and much more compute power. Here is where LRI comes into play: under LRI, we need only consider one PSF per radial distance from the center to compute the forward model. Yet, despite needing far fewer PSFs than the fully shift-varying case, the LRI model produces an identical image for rotationally-symmetric systems.

Moreover, we develop a principled way to estimate the radial stack of PSFs needed for the LRI model from a single image of randomly distributed point sources, e.g., a slide of streaked fluorescent beads. This

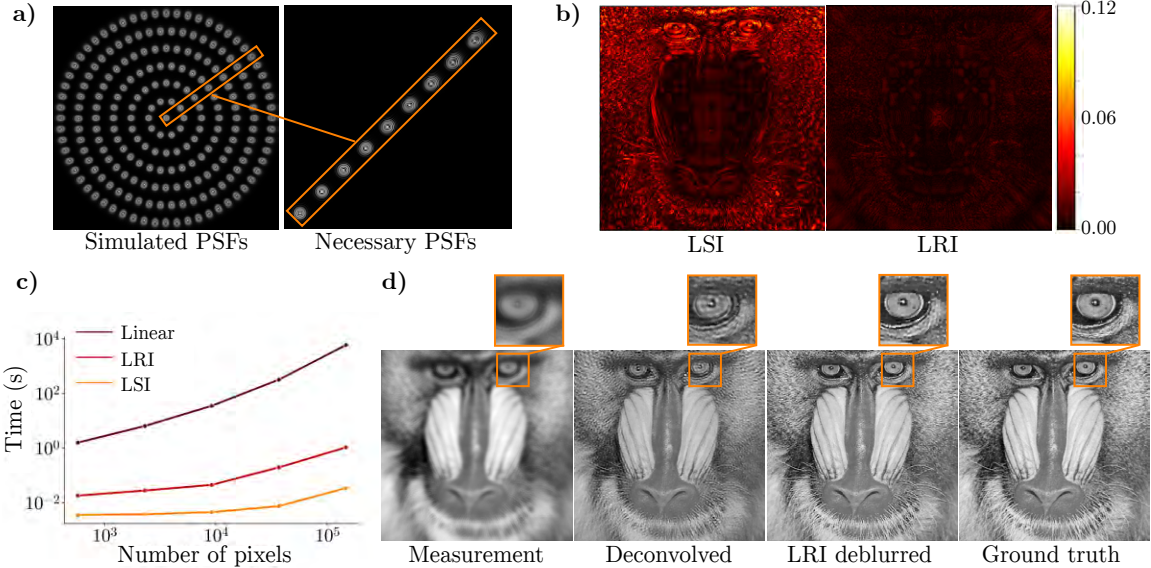


Figure 1: **Overview of LRI forward modeling and deblurring.** **a) Rotationally-symmetric systems are LRI:** using Zemax OpticStudio we simulate the PSFs of a rotationally-symmetric imaging system everywhere in the FoV, finding them to be LRI (their shape only varies radially). The zoom-in shows that only one radial line of PSFs is needed to characterize the system. **b) The LRI forward model is accurate:** we compute the fully shift-varying forward model (using every PSF) and compare it to the LSI and LRI forward models by generating absolute error maps; the LRI forward model is much closer to matching the actual image. **c) The LRI forward model is fast:** shown here is the runtime of each method as a function of image size. Despite being theoretically equivalent to the fully shift-varying model, the LRI model is orders of magnitude faster. **d) LRI deblurring outperforms deconvolution:** we deblur the fully shift-varying measurement using deconvolution and LRI deblurring; note the superior performance of LRI, especially in the corners. Just like deconvolution, LRI deblurring only requires a single calibration image.

strategy reduces the calibration cost of LRI to that of LSI: a single image—albeit with many PSFs in it. In fact, the LRI calibration scheme is more convenient and robust than the LSI calibration scheme, which entails isolating and centering a single point source. After calibrating, we have the necessary PSFs to compute the LRI model, effectively characterizing the imaging system and enabling downstream applications.

The LRI model may find use in many such applications including the frequency analysis (explored in Appendix E) or end-to-end design of imaging systems [1]. However, in this work, we focus on perhaps the most ubiquitous use of a forward model: image deblurring, which amounts to inverting the forward model. In particular, consider inexpensive, large, or small-scale imaging systems subject to shift-varying aberrations (e.g. telescopes, miniature microscopes). Optically correcting such systems may be prohibitively expensive or even impossible, and so we must computationally remedy them using image deblurring. As previously discussed with forward models, such systems cannot be corrected by LSI deconvolution techniques, and shift-varying deblurring methods find little use in practice because their calibration and computation is cumbersome. Instead, we allow engineers to design simple, uncorrected—and consequently aberrated—rotationally-symmetric systems, and correct for their aberrations (i.e., deblur their output image) by properly modeling them with LRI.

To that end, we invert our LRI forward model to deblur the measurements from rotationally-symmetric systems. The algorithm we develop is efficient even for large images and only requires one calibration image (containing multiple PSFs). We validate the LRI forward model and deblurring algorithm in simulation as well as experimentally on images of live tardigrades taken with the UCLA Miniscope v3 [2]. We find that, in simulation, the LRI forward model is nearly identical to the fully shift-varying model with an order of magnitude less complexity. Experimentally, LRI deblurring outperforms deconvolution, especially at the edges of the FoV. Our contributions are exemplified by Fig. 1 and summarized as follows:

1. We introduce the LRI property, derive the LRI forward model, and prove the LRI Convolution Theorem, which form the basis for analyzing rotationally-symmetric imaging systems.
2. We develop practical algorithms for the LRI forward model and LRI deblurring, which inverts the forward model. We provide an accessible Python package which implements these algorithms.
3. We present Seidel calibration, a novel method for calibrating rotationally-symmetric imaging systems based on Seidel aberration coefficients. Using this method, we are able to perform LRI deblurring with a single calibration image per imaging system.
4. We implement LRI deblurring on videos of *in vivo*, fluorescently labeled tardigrades obtained with the UCLA Miniscope v3. We find that LRI deblurring outperforms traditional LSI-based deconvolution.

2 Theory

We begin by formally describing our setting. Let the object plane have coordinates $(u, v) \in \mathbb{R}^2$ and the image plane have coordinates $(x, y) \in \mathbb{R}^2$. Then the final image intensity $f(x, y)$ of a linear optical system is formed by the superposition integral [3]: a weighted sum of PSFs over all object points (u, v) with the form

$$f(x, y) = \int \int g(u, v)h(x, y; u, v)dudv, \quad (1)$$

where $g(u, v)$ describes the object's intensity at (u, v) and $h(x, y; u, v)$ indexes the spatially-varying PSFs; it describes the intensity at (x, y) of the PSF generated by a point source at (u, v) . This equation is the linear image formation model, also known as the system *forward model*—it describes the image as a function of the object. When the PSFs are space-varying, computing this forward model requires measuring the PSF from each object point (u, v) , an impractical task. By placing assumptions on h , we can decrease the number of PSFs needed to compute the model; for example, by assuming the system to be linear shift-invariant, we only need one PSF calibration measurement. The LSI assumption is convenient and often used in practice; however, if the imaging system does not satisfy the chosen assumption, the forward model's accuracy will degrade. In this paper we will introduce a new simplifying assumption, linear revolution-invariance, that works for rotationally-symmetric optical systems. We start by reviewing LSI systems for comparison.

2.1 Linear Shift-Invariance (LSI)

First, we begin with the simplest and most restrictive assumption on h : the linear shift-invariance assumption [4]. Under LSI, the shape of a PSF no longer varies with (u, v) .

Definition 1 (Shift-Invariance). *An imaging system is shift-invariant if*

$$h(x, y; u, v) = h(x - u, y - v; 0, 0).$$

The shape of the PSF does not change as the point source changes location within the FoV. In other words, the image of a point source at (u, v) looks the same as the image of a point source at $(0, 0)$ (i.e., the center PSF), except shifted by (u, v) . Inserting this simplification into the superposition integral (1) yields the convolution integral:

$$f(x, y) = \int \int g(u, v)h(x - u, y - v; 0, 0)dudv = (g * h)(x, y).$$

Computing the LSI model only requires measuring one PSF, so it is practically convenient; however, it ignores any variability in the PSFs that may arise in different parts of the FoV. Applying the convolution theorem allows the frequency spectrum of f to be expressed as a product of the spectra of g and h . This Fourier representation provides the interpretation of an imaging system as a spectral filter. Furthermore, it reduces the computational complexity of the model by a quadratic factor in each dimension via Fast Fourier Transforms (FFTs). Though simple and efficient, the LSI model fails to capture the increased spread of PSFs at the edge of the FoV. This motivates the ensuing derivation of the LRI forward model, which is more accurate than the LSI model but not as onerous as a fully shift-varying model, while being applicable to a wide variety of typical optical systems.

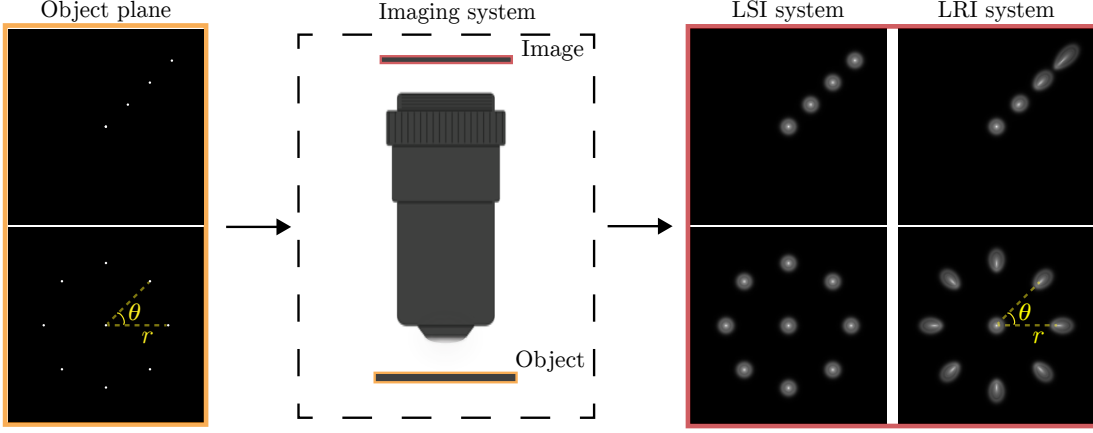


Figure 2: **Linear Revolution-Invariance (LRI).** Consider imaging the point sources (on the left) under LSI and LRI (images shown on the right). For an LSI system, the PSF shape remains the same no matter the location of the point source. For an LRI system, the PSF shapes vary as the point source moves out radially (top row) but remain the same for a fixed radius r and revolve around the center along with the point source (bottom row). If a point rotates an angle θ around the center, then so will its PSF.

2.2 Linear Revolution-Invariance (LRI)

We now make a similar simplification of the PSFs, but instead under the assumption of revolution-invariance. First, let us transform our entire system to polar coordinates; the object and image planes are now indexed by (r, θ) and (ρ, ϕ) respectively. Each of the functions in (1) has a polar counterpart, which we denote with a tilde—for example, define $\tilde{h}(\rho, \phi; r, \theta) = \mathbb{1}_{\{\theta \in (-\pi, \pi]\}} h(\rho \cos \phi, \rho \sin \phi; r \cos \theta, r \sin \theta)$. Note here that we allow θ to vary freely in \mathbb{R} , but the polar function is zero outside $(-\pi, \pi]$. The expressions for \tilde{f}, \tilde{g} are constructed similarly. Recall that, under LRI, if the object rotates with respect to the optical axis by an amount θ_0 , its image also rotates by the same amount, θ_0 . In more familiar terms, LRI can be thought of as *shift-invariance in the angular dimension* θ . See Fig. 2 for a visual explanation.

Definition 2 (Revolution-Invariance). *An imaging system is revolution-invariant if its point spread functions, indexed in polar coordinates by \tilde{h} , satisfy*

$$\tilde{h}(\rho, \phi; r, \theta) = \tilde{h}(\rho, \phi - \theta; r, 0). \quad (2)$$

Note that all optical systems whose physical configuration is symmetric about the optical axis have PSFs satisfying Definition 2. Plugging this modification of h into (1) yields the LRI forward model.

Theorem 1 (LRI Forward Model). *The intensity image of an object g through an LRI system with point spread functions h can be written as*

$$\tilde{f}(\rho, \phi) = \int_0^\infty r \int_{-\infty}^\infty \tilde{g}(r, \theta) \tilde{h}(\rho, \phi - \theta; r) d\theta dr = \int_0^\infty r (\tilde{g} *_{\theta} \tilde{h})(\rho, \phi; r, 0) dr, \quad (3)$$

where $*_{\theta}$ denotes a one dimensional convolution along θ . The LRI operation can be notated as $f \triangleq g \odot h$.

Under LRI, image formation becomes a sum of one-dimensional convolutions along the angular dimension. If we were to cut up the input, output, and PSF images into concentric rings, the LRI forward model computes the output ring at ρ as the superposition of all input rings convolved with the rings at ρ of their corresponding PSFs (see Fig. 3). This ring-wise computation, wherein points at different radii are filtered heterogeneously, is consistent with the underlying intuition in LRI: the blur varies radially. Since the PSFs h no longer depend on θ , it is possible to compute the forward model with PSFs only measured along a single radial line in the FoV. One can apply the LRI assumption and the Fourier Convolution Theorem to (1) to recover an efficient algorithm and a frequency domain interpretation.

Theorem 2 (LRI Convolution Theorem). *Under LRI, where \mathcal{F}_Θ is a one dimensional Fourier transform over θ ,*

$$\tilde{f}(\rho, \phi) = \mathcal{F}_\Theta^{-1} \left\{ \int r \mathcal{F}_\Theta \{\tilde{g}(r, \theta)\} \mathcal{F}_\Theta \{\tilde{h}(\rho, \theta; r)\} dr \right\}(\phi).$$

As with the forward model, the LRI convolution theorem composes the image as a set of concentric rings from the input object which are each uniquely filtered by rings from each PSF. It is worth, for a moment, thinking about the frequencies involved in the computation. These frequencies, which we call *rotational frequencies*, are one-dimensional sinusoidal components along the angular dimension, and describe how the image varies along a ring around the center. An in-depth exploration of rotational frequencies and the Fourier interpretation of the LRI model is provided in Appendix E.

Having developed the LRI forward model, we briefly reflect. For rotationally-symmetric systems, the LRI forward model generalizes the LSI model—that is, any rotationally-symmetric LSI system is also LRI. Also, for rotationally-symmetric systems, it is exact and computationally tractable, so there is no need to run the expensive shift-variant model in (1). One issue remains: in order to evaluate the LRI forward model, we still must measure PSFs at every radius in the FoV (i.e., $\tilde{h}(\rho, \phi; r)$ for all r), a task that may require a motion stage and long calibration times, albeit much shorter than for the fully shift-variant model. However, in Section 3 we will demonstrate a principled technique that allows for the estimation of these requisite PSFs from a single calibration image contains multiple point sources. We then utilize this calibration reduction strategy to operationalize the LRI theory into a practical deblurring algorithm.

3 Methods

In this section we describe practical algorithms based on the theory developed in Section 2. Before we discuss the issue of calibration, we present the discrete analog of the LRI forward model and discuss how to invert it for the purposes of image deblurring.

3.1 LRI Forward Computation

Deblurring under the LRI assumption first requires computing the forward model. To that end, we discretize (3), treating the integral as a sum and replacing each function with a matrix of $N \times N$ pixels. We similarly replace the polar transformation with its discrete counterpart, yielding an $M \times K$ matrix whose rows and columns are angles and radii respectively (see Fig. 3). Each matrix is denoted by the capital letter of the function it discretizes, and the tilde denotes the polar resampled matrix; for example, G is the discretized version of the object g and \tilde{G} is its polar pair. In discrete form, the LRI forward model becomes

$$\tilde{F}_{m,n} = \sum_{j=1}^K \sum_{i=1}^M r_j \tilde{G}_{i,j} \tilde{H}_{m-i,n}^{(j)} = \sum_{j=1}^K r_j (\tilde{G} *_j \tilde{H}^{(j)})_{m,n} \quad (4)$$

Algorithm 1 LRI forward model

Input: $N \times N$ pixel object G ; PSFs along one radial line $H^{(j)}$, $j = 1, \dots, N$; corresponding radii r_j , $j = 1, \dots, N$ for each PSF .

Output: LRI blurred image F

```

1:  $\tilde{G} \leftarrow \text{polarTransform}(G)$                                  $\triangleright$  polar dimensions are  $M \times N$ , angle by radius
2:  $\tilde{F} \leftarrow \text{zeros}(M \times N)$                                 $\triangleright$  initialize the output in polar form as an all zero matrix
3: for  $j = 1, \dots, N$  do
4:    $\tilde{H}^{(j)} \leftarrow \text{polarTransform}(H^{(j)})$ 
5:   for  $i = 1, \dots, N$  do
6:      $\tilde{F}_{:,i} \leftarrow \tilde{F}_{:,i} + r_j \text{iFFT}\{\tilde{G}_{:,j}\} \text{FFT}\{\tilde{H}_{:,i}^{(j)}\}$        $\triangleright$  compute polar output ring by ring
7:    $F \leftarrow \text{inversePolarTransform}(\tilde{F})$ 

```

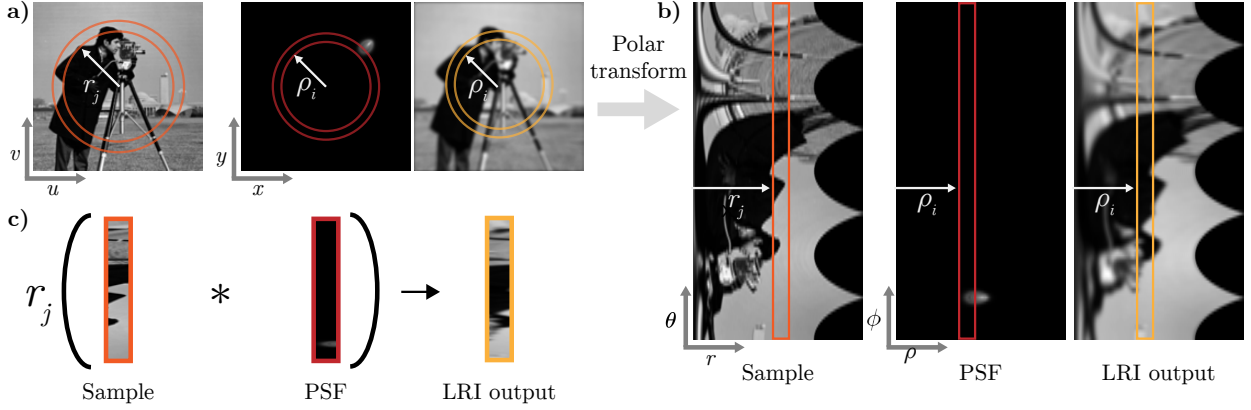


Figure 3: **One iteration of the LRI forward model.** A visual representation of a single term in the LRI forward model. First in a), rings from the sample (orange), the PSF from a point source r_j from the center (red), and the output of the LRI forward model (yellow) are selected. Then in b) after a polar transform these rings become strips. Finally, in c) the output strip at ρ_i adds in the convolution of the object strip at r_j with the PSF strip at ρ_i . See Algorithm 1 for an accompanying description.

where $\tilde{H}^{(j)}$ is the $M \times K$ pixel polar sampled PSF from an object point at radius r_j , and the r_j are evenly spaced radii from the center to the corner of the FoV. The symbol $*_j$ denotes a 1D discrete convolution over the j^{th} matrix column. Thus, the LRI forward model is a sum of one-dimensional convolutions, each of which can be computed via the Fast Fourier Transform (FFT). Algorithm 1 details our implementation of the forward model. Figure 3 is an accompanying visual aid, illustrating one term in the sum from (4). As hinted, computation of this model requires knowledge of K PSFs, one for each radius r_j . In Section 3.3 we demonstrate a technique to recover these K PSFs from a single calibration image as opposed to measuring them directly.

3.2 LRI Deblurring

We perform deblurring by inverting the LRI forward model. An effective method of inversion is to search for a candidate deblurred image \bar{G} such that when passed through the forward model, it best matches the blurry measurement F . For LRI, we frame this approach as the following optimization problem,

$$\hat{G} = \arg \min_{\bar{G} \in \mathbb{R}^{N \times N}} \|F - \bar{G} \circledast H\|_2^2, \quad (5)$$

Notationally, H refers to a collection of PSFs (a set of $N \times N$ matrices) along one radial line, and \circledast now refers to the computation in (4). Since the LRI forward model is linear, this optimization problem is convex in \bar{G} —indeed, it is equivalent to linear least squares—and we solve it using gradient descent. Note, that it is possible to directly invert the LRI model, but an iterative procedure allows us to more easily incorporate image priors (e.g., total variation) and is less memory intensive. Additional details for solving this optimization problem are provided in the appendix.

3.3 Seidel Calibration

The computation of the LRI forward model and deblurring algorithm require H , the collection of PSFs along one radial line in the FoV. Of course, one option is to measure H directly from the system—i.e., measure K images of a point source moving out radially. However, for rotationally-symmetric systems there exists a convenient and compact alternative: fitting the system’s *Seidel aberration coefficients*. These numbers are the coefficients of a rotationally-symmetric polynomial representing the system’s pupil function; their symmetry makes them intrinsically suited for representing LRI systems [5]. Knowing a system’s Seidel coefficients allows one to compute its forward model since they can be used to analytically generate the point spread

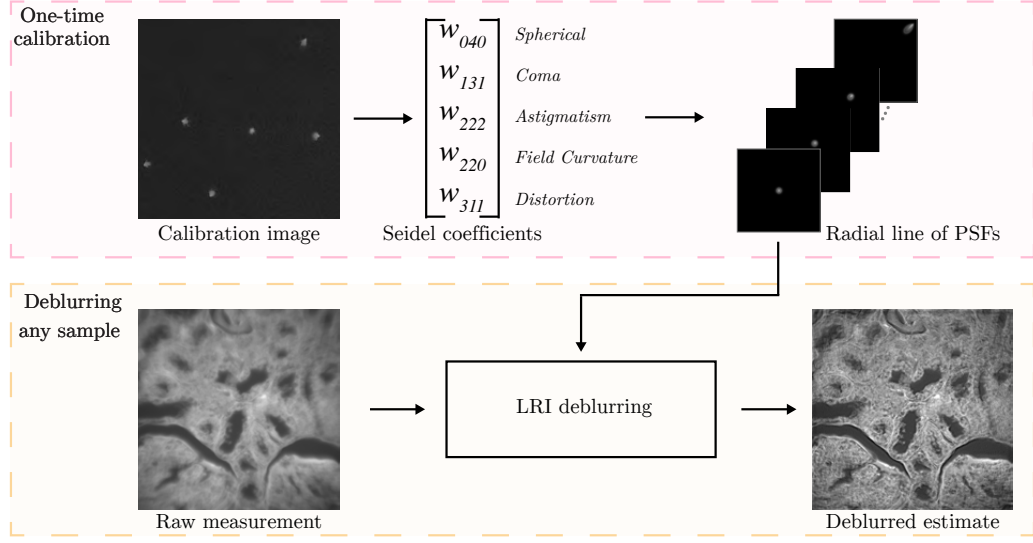


Figure 4: The LRI deblurring pipeline. For each new imaging system of interest, we first calibrate it (top box) by taking an image of a few randomly scattered point sources, fitting the Seidel aberration coefficients, and generating a radial line of PSFs. Then we image a sample, in this case a fixed rabbit liver, and use the generated PSFs to perform LRI deblurring (bottom box). Note the calibration procedure is only needed once per imaging system.

functions H via a Fourier transform (see Appendix D). Another major benefit of this polynomial is that its third-order coefficients—known as the 5 primary Seidel coefficients—index the dominant aberrations present in practical imaging systems: sphere, coma, astigmatism, field curvature, and distortion. By fitting only the primary Seidel coefficients, we reduce the sample complexity of our problem, allowing us to fit the system model with only a single calibration image instead of a set of K PSFs, a procedure we will describe shortly. With these 5 numbers in hand, we can generate all the system’s PSFs with high fidelity.

The estimation procedure for obtaining the 5 primary Seidel coefficients involves fitting them to a single, sparse image of a few randomly scattered point sources (e.g. fluorophores on a microscope slide)—such an image is actually easier to obtain in practice than the an image of an isolated point source in the FoV. This single image simultaneously provides several of the system’s PSFs. Let $\mathcal{R} \subseteq \{1, 2, \dots, K\}$ be the indices of the radii of the points in the calibration image. We then find the primary Seidel coefficients $\hat{\omega}$ whose generated PSFs best match the measured PSFs. Once again, this searching procedure is succinctly stated as an optimization problem,

$$\hat{\omega} = \arg \min_{\bar{\omega} \in \mathbb{R}^5} \sum_{j \in \mathcal{R}} \|H^{(j)} - \mathcal{F}^{-1}\{P(\bar{\omega})^{(j)}\}\|_2^2, \quad (6)$$

where $P(\bar{\omega})^{(j)}$ is an $N \times N$ matrix representing the discretized pupil function with primary Seidel coefficients $\bar{\omega}$ from a point source at distance r_j from the center. Although the problem in (6) is not convex, we obtain reasonable local minima using gradient descent. Armed with the estimated Seidel coefficients, we can generate approximations of the remaining PSFs in H for use in our deblurring algorithm instead of directly measuring them. Figure 4 summarizes this procedure.

It is worth noting that Seidel calibration significantly improves the practical results of both LRI and LSI deblurring because it doubles as a physically-informed denoiser for the PSFs. This added benefit arises because the PSFs that go into the algorithms are synthetically generated and thus have no measurement noise.

4 Results

We implement the LRI forward model, LRI deblurring, and Seidel calibration in code as a Python package, and use it for all subsequent experiments. For fair comparison, all deblurring algorithms are run identically using gradient descent with total variation (TV) regularization until convergence. Further details about the implementation can be found in the Github repository.

4.1 Simulation

First, to verify the validity of the LRI forward model and deblurring algorithms in a controlled setting, we construct a simple simulation. We obtain the simulated PSFs at every FoV point from a simple 4f imaging system modeled in Zemax OpticStudio (see Fig. 1a). The PSFs are LRI but not LSI since they appear to vary only radially. With PSFs in hand, we generate a measurement by superimposing each PSF with the pixels from a test object (in this case, a baboon); this is precisely the fully shift-varying forward model with no additional assumptions (see raw measurement in Fig. 1d).

There are two tasks we execute using the LSI and LRI models: first, we try to best emulate the fully shift-varying measurement—this tests the accuracy of each forward model. Second, to evaluate each model’s deblurring performance, we try to best recover the original test image from the fully shift-varying measurement. In the first task, we generate estimated measurements under LSI and LRI using their respective forward models and display their per-pixel absolute error maps with respect to the fully shift-varying measurement. We also plot the time to generate the measurement under each model as a function of the sidelength (in pixels) of the test image. LRI produces a far more accurate forward measurement than LSI at the cost of increased compute time, though it is still far more efficient than the fully shift-varying reference (LRI is $\mathcal{O}(N^3 \log(N))$ while the fully shift-varying model is $\mathcal{O}(N^4)$). In the second task, we run LSI and LRI deblurring on the fully shift-varying measurement using identical optimization procedures and display the deblurred results in Fig. 1d. While both methods considerably sharpen the measurement, the LRI method provides better deblurring across the image, especially the corners. These results imply an expected result: since the PSFs were indeed LRI, the LRI-based computations efficiently incorporated the additional information of a radial line of PSFs and outperformed the LSI-based methods outside of the center of the FoV where shift-invariance is no longer true.

4.2 Experiments

Next, we calibrate a UCLA Miniscope v3 fluorescent microscope and use it to image and deblur a variety of samples, including live videos of tardigrades. This process is summarized in Fig. 4: we first take a single image of a few $1\mu m$ fluorescent beads—surrogate point sources—at different radii. Note that the image in Fig. 4 reveals that the Miniscope is approximately LRI. We use this single image to fit Seidel aberration coefficients and subsequently generate the remaining line of PSFs needed to compute perform LRI deblurring. It is worth noting that the Seidel calibration procedure has the added benefit of denoising the observed PSFs in a structured way; it replaces noisy, experimentally captured PSFs with noiseless, simulated surrogates. Now we image any number of samples of interest, yielding a set of blurry measurements. Finally, we apply the LRI deblurring algorithm using our line of PSFs to obtain a deblurred estimate of each sample. This procedure can be generalized to *any* rotationally-symmetric imaging system—of course, the surrogate for point sources may be different, such as stars for telescopes.

USAF resolution target. After calibration, we image a USAF resolution target placed at 9 separate locations in the FoV, forming a uniform grid. This was done so that we could observe the highest resolution groups (i.e., those greater than group 8) in each part of the FoV. We stitch these 9 images together, using only the region of each constituent image that contains the high resolution group, in order to form the raw measurement shown in Fig. 5. We then perform LSI and LRI deblurring of the raw measurement and find that, much like in simulation, the LRI method deblurs the measurement more consistently across the FoV, revealing greater details in the outer panels of the image. We encourage the reader to see this by comparing LSI and LRI panel-by-panel in Fig. 5.

Mouse liver tissue. For our next experiment, we image microscope slides of mouse liver tissue. After LRI deblurring, key features of the tissue are revealed in the corners of the image, including the outlines of

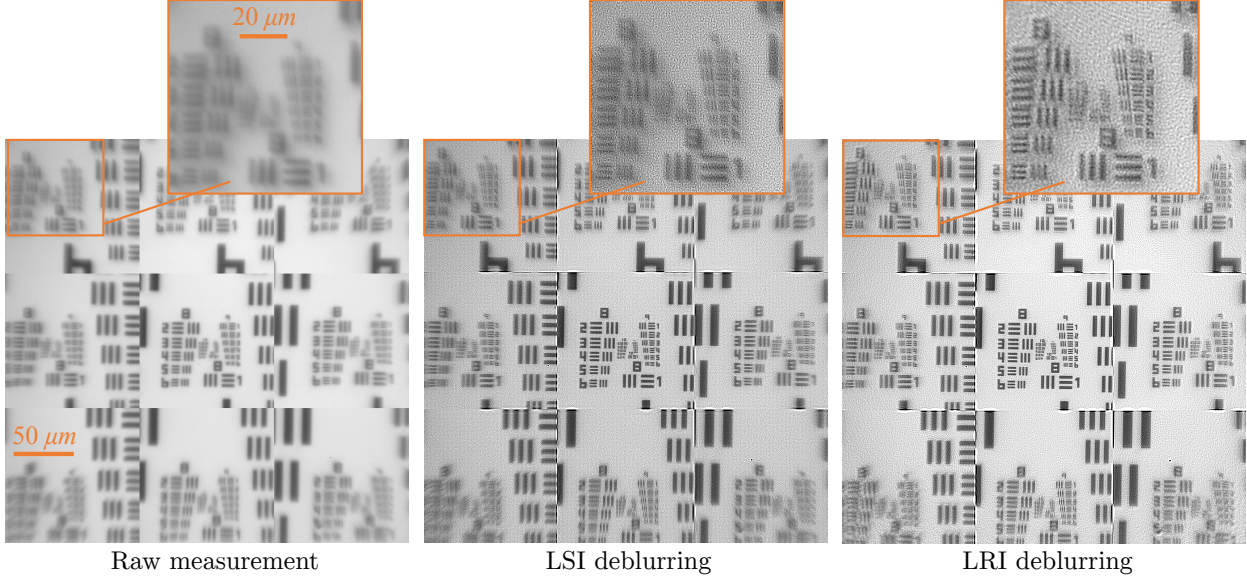


Figure 5: Deblurring of composited resolution targets. We stitched together images of a resolution target taken with the Miniscope v3 at different locations in the FoV resulting in the raw measurement shown on the left. We then performed LSI deblurring (middle) and LRI deblurring (right) using single-shot Seidel calibration. Note that LRI outperforms LSI in the outer panels, especially those in the corners of the image.

membranes, which are not visible in the raw measurement or after LSI deblurring. See Fig. 4 for the LRI deblurred image and Fig. 7 in the appendix for additional images and direct comparison to LSI.

Live tardigrades. For our final experiment we fluorescently label live, semi-starved tardigrades with a DNA gel stain, and capture a series of videos. We apply both LSI and LRI deblurring to each frame and display a few of them in Fig. 6; the full videos can be found here. As with the previous experiments, the LRI deblurring provides increased image contrast and detail in the corners of the frames as compared to LSI deblurring. In particular, with LRI deblurring, the small, dot-like features within the tardigrade are better resolved.

5 Discussion

We develop a new way to model image formation using the practically informed assumption that imaging systems are rotationally-symmetric. We characterize corresponding effect of rotational symmetry on the point spread functions of these systems, yielding the linear revolution-invariance (LRI) assumption. Under LRI, we experimentally demonstrate an improved capability to accurately model image formation and perform image deblurring. Beyond deblurring, we mark this as the beginning of a re-exploration of the many theoretical ideas and practical algorithms which have long been rooted in the shift-invariance assumption, such as optical transfer functions, the idea that lenses take Fourier transforms, quantifying resolution, *et cetera*. In addition to providing a theoretical foundation for imaging through rotationally-symmetric optical systems, LRI may improve the performance of LSI in other applications—for example, co-designing simpler and higher-resolution optical systems with the LRI deblurring algorithm. Finally, we believe the LRI assumption can be combined with hybrid deep-learning-analytical approaches (as per [6] in order to speed up and/or enhance its deblurring capabilities.

6 Related Work

The idea of linear shift-invariance—or rather its 1D predecessor time invariance—is difficult to trace historically, but the first mention of it that we were able to find was by Richard Hamming in 1934 [7], followed by

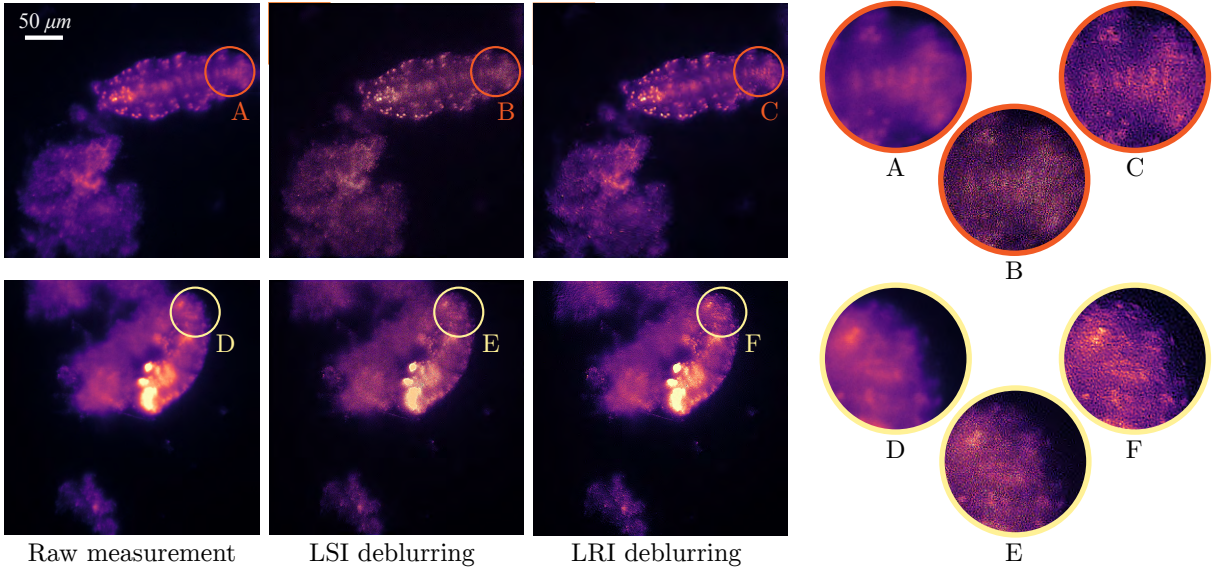


Figure 6: **Deblurring of *in vivo* tardigrades.** Two example frames from captured videos of live tardigrades are shown here with the raw measurement (left), LSI deblurred image (middle), and LRI deblurred image (right). Also pictured are zoom-ins of specific regions of each frame. Note that LRI deblurring has higher contrast and better resolves smaller features near the image corners as compared with LSI deblurring.

the far more popular definition provided in [4]. The concept also has a close connection to the convolution integral—which had existed separately as far back as the 1800s [8]—through the famous Convolution Theorem. Much of the foundational mathematics of convolution and its frequency domain interpretation comes from the work of Laplace and Fourier; these techniques enabled the application of linear time (shift)-invariant systems to communications and, of course, imaging. The practical use of LSI systems for imaging analysis arose from Bell labs during the emergence of digital signal processing for communication in the 1960s and 1970s.

Image deblurring has its roots much later; it was only in 1949 when Norbert Wiener published the Wiener Filter for linear time-invariant deconvolution [9]. While the original technique was developed in 1940 for time series data in order to track enemy planes in World War II, it was soon adapted for image deblurring. With the rise of digital computing in the following decades came an explosion of image deconvolution techniques which are commonly employed today such as Richardson-Lucy [10, 11]. It is interesting to note that some of these algorithms have existed for nearly a century and yet there is no clear “best” method.

More recently, deconvolution has been generalized to deblurring spatially varying systems. A wide array of such techniques attempt to simplify the spatially varying image formation model in different ways such as: assuming each region of an image is locally LSI [12], interpolating PSFs [13, 14], decomposing the PSF into shift-invariant orthogonal modes [15–21], doing the same in Fourier space [22], quantifying the degree of shift variance [23, 24], and using deep learning [6, 25]. Despite the ever growing pool of techniques, shift-varying deblurring has not become commonplace among practitioners as it is difficult to calibrate and computationally expensive.

The aforementioned models and deblurring techniques do not explicitly utilize the rotational symmetry naturally present in most optics. However, a significant portion of optical theory is developed under the assumption of rotational symmetry; for example, the analysis of an optical system while considering only a single plane is only possible assuming rotational symmetry. The use of rotational symmetry and polar transformations for deblurring arises in modeling motion blur [26, 27], suppressing radial variance [28], and segmenting the FoV into shift-invariant radial segments [29–32]. Additionally, ray models have been developed using Seidel coefficients [33]. Many of these works are beating around the bush of LRI, although none rigorously define it or develop algorithms with accompanying theoretical analysis.

References

- [1] E. Tseng, A. Mosleh, F. Mannan, K. St-Arnaud, A. Sharma, Y. Peng, A. Braun, D. Nowrouzezahrai, J.-F. Lalonde, and F. Heide, "Differentiable compound optics and processing pipeline optimization for end-to-end camera design," *ACM Transactions on Graphics (TOG)*, vol. 40, no. 2, pp. 1–19, 2021.
- [2] D. Aharoni, *Ucla miniscope*. [Online]. Available: http://www.miniscope.org/index.php/Main_Page.
- [3] J. W. Goodman, "Introduction to fourier optics. 3rd," *Roberts and Company Publishers*, 2005.
- [4] A. V. Oppenheim and R. W. Schafer, "Digital signal processing(book)," *Research supported by the Massachusetts Institute of Technology, Bell Telephone Laboratories, and Guggenheim Foundation. Englewood Cliffs, N. J., Prentice-Hall, Inc., 1975. 598 p*, 1975.
- [5] M. Born and E. Wolf, *Principles of optics: electromagnetic theory of propagation, interference and diffraction of light*. Elsevier, 2013.
- [6] K. Yanny, K. Monakhova, R. W. Shuai, and L. Waller, "Deep learning for fast spatially varying deconvolution," *Optica*, vol. 9, no. 1, pp. 96–99, 2022. DOI: 10.1364/OPTICA.442438. [Online]. Available: <http://opg.optica.org/optica/abstract.cfm?URI=optica-9-1-96>.
- [7] U. S. N. B. of Standards, *Miscellaneous Publication - National Bureau of Standards*, ser. Miscellaneous Publication - National Bureau of Standards. The Bureau, 1934. [Online]. Available: <https://books.google.com/books?id=Cct0OyTHR3QC>.
- [8] A. Dominguez, *A history of the convolution operation*, 2015. [Online]. Available: <https://www.embs.org/pulse/articles/history-convolution-operation/>.
- [9] N. Wiener *et al.*, *Extrapolation, interpolation, and smoothing of stationary time series: with engineering applications*. MIT press Cambridge, MA: 1964, vol. 8.
- [10] W. H. Richardson, "Bayesian-based iterative method of image restoration," *J. Opt. Soc. Am.*, vol. 62, no. 1, pp. 55–59, 1972. DOI: 10.1364/JOSA.62.000055. [Online]. Available: <http://opg.optica.org/abstract.cfm?URI=josa-62-1-55>.
- [11] L. Lucy, "An iterative technique for the rectification of observed distributions," *Astronomical Journal*, vol. 79, p. 745, 1974. DOI: 10.1086/111605.
- [12] H. Trussell and B. Hunt, "Image restoration of space variant blurs by sectioned methods," in *ICASSP '78. IEEE International Conference on Acoustics, Speech, and Signal Processing*, vol. 3, 1978, pp. 196–198. DOI: 10.1109/ICASSP.1978.1170472.
- [13] L. Denis, E. Thiébaut, and F. Soulez, "Fast model of space-variant blurring and its application to deconvolution in astronomy," in *2011 18th IEEE International Conference on Image Processing*, 2011, pp. 2817–2820. DOI: 10.1109/ICIP.2011.6116257.
- [14] J. G. Nagy and D. P. O'Leary, "Restoring images degraded by spatially variant blur," *SIAM Journal on Scientific Computing*, vol. 19, no. 4, pp. 1063–1082, 1998. DOI: 10.1137/S106482759528507X. [Online]. Available: <https://doi.org/10.1137/S106482759528507X>.
- [15] L. Denis, E. Thiébaut, F. Soulez, J.-M. Becker, and R. Mourya, "Fast approximations of shift-variant blur," *International Journal of Computer Vision*, vol. 115, no. 3, pp. 253–278, 2015.
- [16] R. C. Flicker and F. J. Rigaut, "Anisoplanatic deconvolution of adaptive optics images," *J. Opt. Soc. Am. A*, vol. 22, no. 3, pp. 504–513, 2005. DOI: 10.1364/JOSAA.22.000504. [Online]. Available: <http://opg.optica.org/josaa/abstract.cfm?URI=josaa-22-3-504>.
- [17] H. Deng, W. Zuo, H. Zhang, and D. Zhang, "An additive convolution model for fast restoration of nonuniform blurred images," English, *International Journal of Computer Mathematics*, vol. 91, no. 11, pp. 2446–2466, 2014. DOI: 10.1080/00207160.2013.811235.
- [18] D. Miraut and J. Portilla, "Efficient shift-variant image restoration using deformable filtering (part i)," *EURASIP Journal on Advances in Signal Processing*, vol. 2012, no. 1, pp. 1–20, 2012.
- [19] T. Popkin, A. Cavallaro, and D. Hands, "Accurate and efficient method for smoothly space-variant gaussian blurring," *IEEE Transactions on image processing*, vol. 19, no. 5, pp. 1362–1370, 2010.

- [20] F. Sroubek, J. Kamenicky, and Y. M. Lu, “Decomposition of space-variant blur in image deconvolution,” *IEEE Signal Processing Letters*, vol. 23, no. 3, pp. 346–350, 2016. DOI: 10.1109/LSP.2016.2519764.
- [21] T. Lauer, “Deconvolution with a spatially variant PSF,” in *Astronomical Data Analysis II*, J.-L. Starck and F. D. Murtagh, Eds., International Society for Optics and Photonics, vol. 4847, SPIE, 2002, pp. 167 –173. DOI: 10.1117/12.461035. [Online]. Available: <https://doi.org/10.1117/12.461035>.
- [22] S. Lee, K. Lee, S. Shin, and Y. Park, “Generalized image deconvolution by exploiting the transmission matrix of an optical imaging system,” *Scientific Reports*, vol. 7, no. 1, pp. 1–10, 2017.
- [23] S.-H. Lin, T. F. Krile, and J. F. Walkup, “Piecewise isoplanatic modeling of space-variant linear systems,” *J. Opt. Soc. Am. A*, vol. 4, no. 3, pp. 481–487, 1987. DOI: 10.1364/JOSAA.4.000481. [Online]. Available: <http://opg.optica.org/josaa/abstract.cfm?URI=josaa-4-3-481>.
- [24] A. W. Lohmann and D. P. Paris, “Space-variant image formation,” *J. Opt. Soc. Am.*, vol. 55, no. 8, pp. 1007–1013, 1965. DOI: 10.1364/JOSA.55.001007. [Online]. Available: <http://opg.optica.org/abstract.cfm?URI=josa-55-8-1007>.
- [25] O. Ronneberger, P. Fischer, and T. Brox, “U-Net: Convolutional networks for biomedical image segmentation,” in *International Conference on Medical Image Computing and Computer-Assisted Intervention*, Springer, 2015, pp. 234–241.
- [26] C. B. Webster and S. J. Reeves, “Radial deblurring with ffts,” in *2007 IEEE International Conference on Image Processing*, vol. 1, 2007, pp. I –101–I –104. DOI: 10.1109/ICIP.2007.4378901.
- [27] G. Boracchi, A. Foi, V. Katkovnik, and K. Egiazarian, “Deblurring noisy radial-blurred images: Spatially adaptive filtering approach,” in *Image Processing: Algorithms and Systems VI*, International Society for Optics and Photonics, vol. 6812, 2008, p. 68121D.
- [28] S. Luan, S. Xie, T. Wang, X. Hao, M. Yang, and Y. Li, “A space-variant deblur method for focal-plane microwave imaging,” *Applied Sciences*, vol. 8, no. 11, p. 2166, 2018.
- [29] Y. Zhang and T. Ueda, “Deblur of radially variant blurred image for single lens system,” *IEEJ Transactions on Electrical and Electronic Engineering*, vol. 6, no. S1, S7–S16, 2011. DOI: <https://doi.org/10.1002/tee.20615>. [Online]. Available: <https://onlinelibrary.wiley.com/doi/abs/10.1002/tee.20615>.
- [30] Y. Zhang, I. Minema, and T. Ueda, “Restoration of radially blurred image created by spherical single lens system of cell phone camera,” *Proceedings of IEEE Sensors*, pp. 1333–1337, 2010. DOI: 10.1109/ICSENS.2010.5690562.
- [31] Y. Zhang, I. Minema, L. G. Zimin, and T. Ueda, “Analysis of radially restored images for spherical single lens cellphone camera,” *IEEE Sensors Journal*, vol. 11, no. 11, pp. 2834–2844, 2011. DOI: 10.1109/JSEN.2011.2167504.
- [32] Y. Zhang, L. G. Zimin, J. Ji, S. Ikezawa, and T. Ueda, “Real scene capturing using spherical single-element lens camera and improved restoration algorithm for radially variant blur,” *Opt. Express*, vol. 20, no. 25, pp. 27569–27588, 2012. DOI: 10.1364/OE.20.027569. [Online]. Available: <http://opg.optica.org/oe/abstract.cfm?URI=oe-20-25-27569>.
- [33] C. Wang, J. Chen, H. Jia, B. Shi, R. Zhu, Q. Wei, L. Yu, and M. Ge, “Parameterized modeling of spatially varying psf for lens aberration and defocus,” *J. Opt. Soc. Korea*, vol. 19, no. 2, pp. 136–143, 2015. [Online]. Available: <http://opg.optica.org/josk/abstract.cfm?URI=josk-19-2-136>.
- [34] D. P. Kingma and J. Ba, “Adam: A method for stochastic optimization,” *arXiv:1412.6980*, 2014.
- [35] D. G. Voelz, *Computational fourier optics: a MATLAB tutorial*. SPIE press Bellingham, Washington, 2011.

A Proofs

Proof. Rewriting (1) in polar coordinates gives

$$\tilde{f}(\rho, \phi) = \int_0^\infty r \int_{-\pi}^{\pi} \tilde{g}(r, \theta) \tilde{h}(\rho, \phi; r, \theta) d\theta dr$$

Applying the LRI assumption (2) to the right-hand side above and replacing the limits of the inner integral with an indicator function yields a convolution over θ

$$\tilde{f}(\rho, \phi) = \int_0^\infty r \int_{-\infty}^{\infty} \tilde{g}(r, \theta) \tilde{h}(\rho, \phi - \theta; r) d\theta dr = \int_0^\infty r (\tilde{g} *_{\theta} \tilde{h})(\rho, \phi; r, 0) dr. \blacksquare$$

Proof. Note that given the nature of this paper, in the theorem statement and throughout the paper we neglect certain measure-theoretic niceties such as well-temperedness or absolute integrability. Since the given system is LRI, (3) holds. Applying the Fourier Convolution Theorem to the one dimensional convolution on the right-hand side of (3) yields

$$\tilde{f}(\rho, \phi) = \int r \mathcal{F}_\Theta^{-1} \left\{ \mathcal{F}_\Theta \{ \tilde{g}(r, \theta) \} \mathcal{F}_\Theta \{ \tilde{h}(\rho, \theta; r) \} \right\}(\phi) dr,$$

where \mathcal{F}_Θ is the one dimensional Fourier transform over θ . By Fubini's theorem, we pull the inverse Fourier Transform outside of the integral, which gives

$$\tilde{f}(\rho, \phi) = \mathcal{F}_\Theta^{-1} \left\{ \int r \mathcal{F}_\Theta \{ \tilde{g}(r, \theta) \} \mathcal{F}_\Theta \{ \tilde{h}(\rho, \theta; r) \} dr \right\}(\phi). \blacksquare$$

B Additional Results

The tardigrade images shown in the main manuscript are single frames from a series of short videos taken using the Miniscope. We apply LSI and LRI deblurring frame-by-frame to these videos. Here we provide a link to the raw, LSI deblurred, and LRI deblurred videos for comparison. Just like the individual frame results presented in the paper, the LRI video has more contrast and clarity near the corners than the LSI video.

Figure 7 contains a few additional experimental results using the same procedure and setup outlined above as well as in 4.2. These results contain images of rabbit liver tissue and insect cornea which are deblurred under the LSI and LRI assumptions. The features at edges and corners of these images are visible with LRI deblurring; e.g., the membrane-like structures in the liver tissue and the tessellation edges in the cornea.

C Experimental Details

Here we outline the specific details of our sample preparation, imaging setup, and computation.

C.1 Sample Preparation

A mixture of starved and nonstarved tardigrades were stained overnight with an Invitrogen nucleic acid gel fluorescent stain whose excitation and emission maxima are 502 nm and 530 nm respectively. Individual stained tardigrades were then isolated onto a glass slide for imaging. Meanwhile, the non-fluorescent samples (USAF resolution targets, rabbit liver tissue, and insect cornea) were obtained imaging-ready on glass slides.

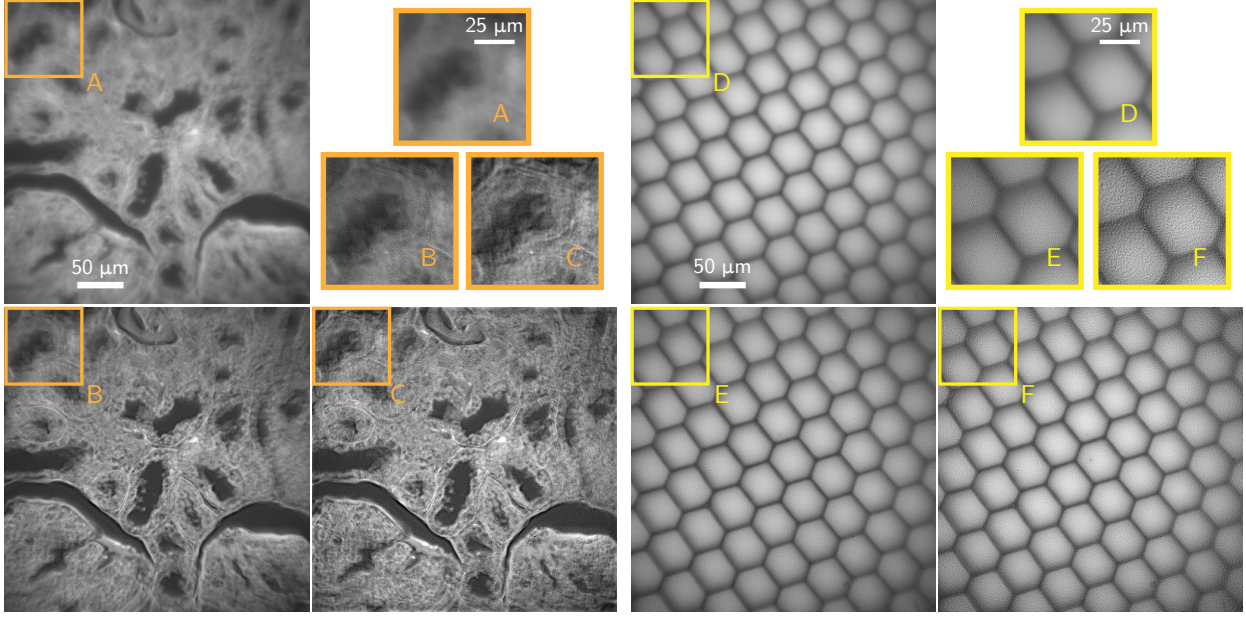


Figure 7: Deblurring of non-fluorescent samples. Thin slices of rabbit liver tissue (left half) and insect cornea (right half) are imaged, producing blurry measurements (top), and deblurred using LSI (bottom left) and LRI (bottom right). LRI deblurring provides high contrast and effective resolution than LSI in the corners of the image; this result is displayed by the zoom-ins for the raw measurement, LSI deblur, and LRI deblur shown by A,B,C for the rabbit liver tissue and D,E,F for the insect cornea, respectively.

C.2 Imaging

For all imaging experiments, we used the Miniscope v3 with the Ximea MU9PM-MBRD 12 bit, 2.2 micron pixel sensor. Optically, the Miniscope is comprised of a gradient index objective and achromat tube lens; further details are provided in [2]. In order obtain the system point spread functions, we imaged 1 micron fluorescent beads smeared on a glass slide. For LSI calibration we iteratively diluted the bead solution with isopropyl alcohol until we were able to sufficiently isolate a single bead, whereas for LRI calibration we used a single dilution and imaged a slide containing a sparse collection of beads.

C.3 Computation

Point spread function generation for the simulation experiments was done by modeling the Miniscope v3 in Zemax OpticStudio (see the Github for a zemax file). The remaining computation was done using Python on a single Nvidia GeForce GPU.

Both the LSI and LRI deblurring models are equivalent to linear least squares optimization problems (see (5)) but we additionally add TV regularization and consequently solve them iteratively till convergence using an ADAM optimizer [34]. For each method, the hyperparameters—including learning rate and regularization strength—that provided the smallest loss and best qualitative results were used. Note that alternative methods for LSI deblurring, such as Wiener and Richardson-Lucy deconvolution, were performed, but yielded strictly worse results than the gradient-based iterative solution with TV regularization.

Further implementation details of the LRI forward model, polar transform, Seidel fitting, and LRI deblurring can be found in the codebase. Beyond implementation details to understand the method, our intent is for this codebase to function as a easy-to-use library such that any practitioner with any imaging system can perform LRI deblurring with only a single calibration image and raw measurement in hand.

D Seidel Coefficients

There exists an alternative characterization of an LRI system: the Seidel aberration coefficients. If known, these numbers allow for the synthetic generation of PSFs from rotationally-symmetric systems, and are thereby adequate to compute the LRI forward model. Here, we give a brief background on Seidel coefficients. This is not a complete treatment and we encourage an interested reader to refer to [35] for an overview, and the standard [5] for a fully rigorous derivation.

Consider an LRI imaging system. It is common to consolidate the system aberrations into a single function and apply it at the exit pupil plane of the system. This complex-valued function, known as the generalized pupil function p is composed of a binary-valued amplitude distribution (set by the shape of the pupil) and a phase distribution w , which quantifies the deviation of the pupil wavefront from the ideal spherical shape necessary for diffraction-limited imaging. Since LRI systems are generally shift-varying (albeit only radially), w becomes a function of the distance of the source from the optical axis r . Letting (s, t) be the pupil plane coordinates, we can write p as

$$p(s, t; r) = \text{circ}\left(\frac{r}{R}\right)e^{w(s, t; r)}.$$

For rotationally-symmetric systems, as in our case, it is possible to expand w as an infinite power series (see the aberration function in [5]). Usually only the third-order terms of this series are used which yields the following 2D polynomial of the pupil plane coordinates,

$$w_\omega(s, t; r) = \omega_s(s^2 + t^2)^2 + \omega_c(s^2 + t^2)sr + \omega_a s^2 r^2 + \omega_f(s^2 + t^2)r^2 + \omega_d s r^3,$$

where $\omega = (\omega_s, \omega_c, \omega_a, \omega_f, \omega_d)$ are the five primary Seidel coefficients and w_ω only depends on the radial location due to the LRI assumption. Note that while the 5 primary Seidel coefficients are a subset of the infinitely many available coefficients, they represent the most common optical aberrations: spherical, coma, astigmatism, field curvature, and distortion. In particular, these aberrations are inherent to all spherically-shaped optics. Finally, it is no coincidence that the pupil function and PSFs both characterize system imperfections; they are related by the Fourier transform,

$$h(x, y; r) = |\mathcal{F}^{-1}\{p(-\lambda df_x, -\lambda df_y; r)\}|^2,$$

where λ is the wavelength of light, d is the distance from the pupil plane to the image plane, and f_x, f_y are the variables which the Fourier transform is taken over. Knowledge of the 5 Seidel coefficients provides an approximation of the pupil function, which in turn, can accurately estimate PSFs for LRI system, including the radial line of PSFs needed for computing the LRI forward model.

E A Fourier Interpretation of LRI

Perhaps the main reason to make the linear shift-invariant assumption is access to its Fourier space pair. Through an application of the Convolution Theorem to 2.1, we see that an LSI system's output spectrum is a product of the input's spectrum with the spectrum of the impulse response, i.e., the transfer function. Thus any LSI imaging system can be thought of as a *filter* which individually scales each frequency component of the input object's intensity distribution. In the context of imaging, the transfer function—now called the Optical Transfer Function (OTF)—is image-valued and describes how the imaging system scales each spatial frequency in the sample. The OTF gives rise to valuable intuitions; for example, since all practical imaging systems have bandlimited transfer functions, the output image is a lowpass-filtered, blurry version of the sample whose resolution is directly proportional to the bandlimit.

In the following text we will formally develop an analogous Fourier interpretation of the LRI image formation model and explain how its features can similarly be used to characterize the performance of an imaging system. While the LRI interpretation is more complicated than its LSI counterpart, it provides a richer and more realistic view of how imaging systems transmit frequencies. As an example of its utility, we will see that the LRI model allows for a more general, radially dependent notion of system resolution.

To begin, we will define a slightly different notion of spatial frequency, called rotational frequency, which is the key quantity that is altered in an LRI system. The rotational frequency is notated as Θ in the following definition.

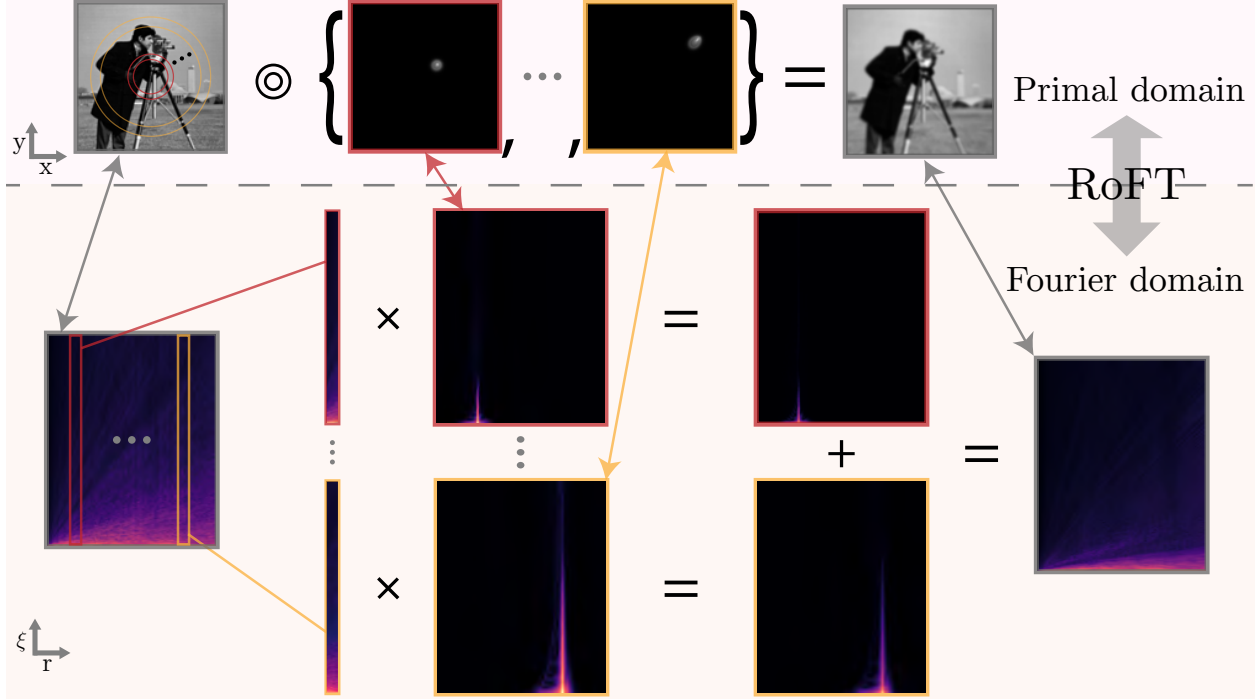


Figure 8: **LRI filtering.** On the top, pink box is the primal LRI filtering: An object (left) is LRI filtered by a radial set of PSFs (middle) to give a blurry image (right). The bottom, orange box shows the Fourier equivalent. Double arrows indicate Rotational Fourier Transform (RoFT) pairs. Strips at each r of the object RoFT (left) are individually multiplied by the RoFTs of the corresponding PSF at r (middle left) producing filtered contributions (middle right). Finally each of these contributions for every r is summed to form the RoFT of the blurry image (right).

Definition 3 (Rotational Fourier Transform (RoFT)). *Let $f : \mathbb{R}^2 \rightarrow \mathbb{C}$ represent a (potentially complex-valued) image, and let \tilde{f} be its polar counterpart (as per Section 2). The RoFT of f is given by*

$$\tilde{F}(r, \xi) = \int \tilde{f}(r, \theta) e^{i2\pi\theta\xi} d\theta.$$

Intuitively, one can think of the values of rotational frequencies as quantifying how quickly the image can change as one travels in a ring of radius r around the center. However, this notion of oscillation speed depends on the radius—think about the spokes on the wheel of a bicycle, even though the spokes are evenly spaced for any given radius, they become further spaced for larger radii. However, under polar sampling they are scaled to have the same frequency. This scaling can be seen in Fig. 8 as the RoFT of each quantity tend to have higher frequencies at larger radii.

Now, writing the LRI convolution theorem in terms of the RoFTs of each quantity (denoted with capital letter and tilde), we see that

$$\tilde{F}(\rho, \xi) = \int r \tilde{G}(r, \xi) \tilde{H}(\rho, \xi; r) dr.$$

Like its LSI counterpart, the above model can be thought of a filtering operation, but now a more complex one; the object’s values r away from the center are *filtered* and *mixed* by the r^{th} PSF. To more fully understand this interpretation, consider the object’s values at some radius r ; they form a ring which will be filtered by the r^{th} PSF. Specifically, spectrum of this ring, or equivalently its RoFT at r , is pointwise multiplied by each ring in the RoFT of the r^{th} PSF, which yields a set of filtered rings indexed by ρ . The ρ^{th} filtered ring represents the contribution of the object ring at r to the image ring at ρ . Figure 8 summarizes this process.

It follows that the r^{th} PSF determines not only what strength of the object’s rotational frequencies end up in the image but also where they are mixed in the image. By looking at the shape r^{th} PSF we can

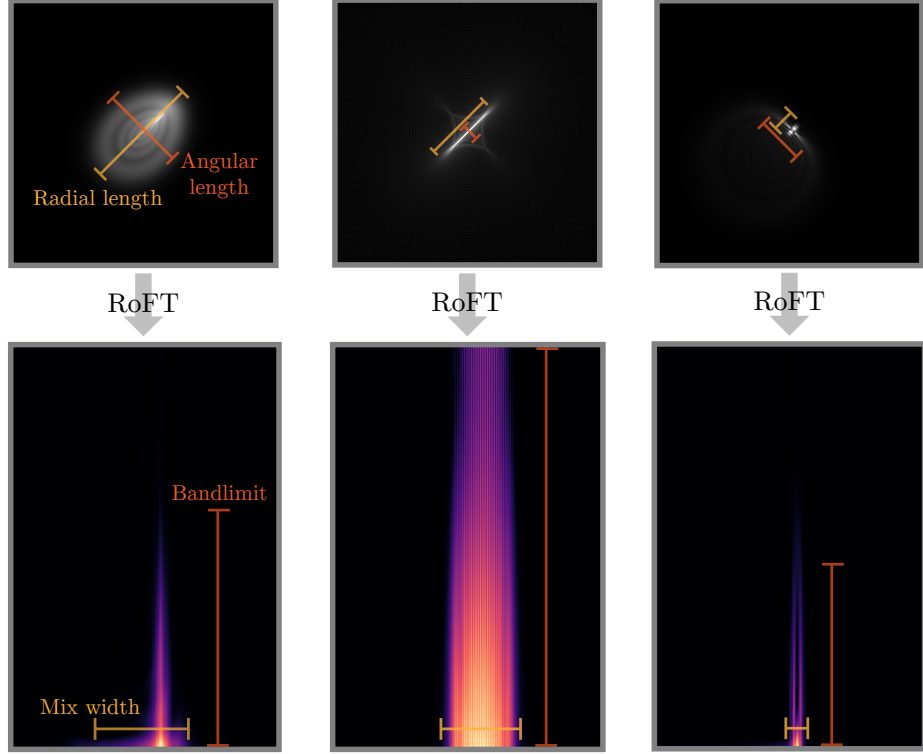


Figure 9: **LRI PSF interpretation.** Evaluating an LRI optical system amounts to considering the length of each PSF in the angular and radial directions. These lengths are inversely proportional to the bandwidth and mix width of the corresponding RoFT, respectively (see leftmost column). In the middle column we see an elongated PSF in the radial direction (i.e., astigmatism) which has a large bandwidth, but incurs more off-radius mixing due to a large mix width. The rightmost column shows an elongated PSF in the angular direction which will have a small mix width, but has a relatively small bandwidth.

determine the exact nature of this filtering and mixing. As shown in Fig. 9 the angular length of the PSF determines the height of the PSF’s RTF at ρ , which tells us which of the object rotational frequencies at r will make it to the image at ρ —this is analogous to the OTF bandwidth in the LSI case. Meanwhile, the radial extent of the PSF (i.e., how many concentric rings it covers) controls the extent of the image rings (i.e., which ρ values) are effected by the object at r . This manifests as the width of the PSF’s RoFT which we call the *mix width*.

Now our notion of resolution, assuming the ability to perfectly de-mix, is radially dependent and, at radius r , is proportional to the angular arc length at $\rho = r$ of the r^{th} PSF. The LRI filtering interpretation offers a more realistic understanding of how an imaging system filters an object and opens the door for a host of new imaging techniques which optimize for key features, such as resolution, under the LRI model.